

Adaptive Acquisition and Tracking for Deep Space Array Feed Antenna Systems

Ryan Mukai, Victor A. Vilnrotter, *Member IEEE*

Payman Arabshahi, *Member IEEE*, and Vahraz Jamnejad

California Institute of Technology
Jet Propulsion Laboratory
4800 Oak Grove Drive, MS 238-343
Pasadena, CA 91109 USA
Tel: (818) 393-6054
Email: payman@fermi.jpl.nasa.gov

Abstract

The use of radial basis function networks and least squares algorithms for acquisition, and fine tracking of NASA's 70-meter deep space network antennas is described and evaluated. We demonstrate that such an RBF network, working in conjunction with an array feed compensation system, and trained using the computationally efficient orthogonal least-squares algorithm, can point a 70-meter deep space antenna with RMS errors of 0.1-0.5 millidegree, under a wide range of signal-to-noise-ratios and antenna elevations, achieving significantly higher accuracies than the 0.8 millidegree benchmark for communications at Ka-band frequencies of 32 GHz. Continuous adaptation strategies for the RBF network were also implemented to compensate for antenna aging, thermal gradients, and other factors leading to time-varying changes in the antenna structure, resulting in dramatic improvements in system performance. The system described here is currently in testing phases at NASA's Goldstone DSN station, and slated for implementation for real-time, adaptive acquisition and tracking of the antenna, marking the first real example of a computationally intelligent telecommunication application for NASA's deep space network.

1 Introduction

The NASA Deep Space Network - or DSN - is an international network of steerable, high-gain reflector antennas, which supports interplanetary spacecraft missions, radio and radar astronomy observations for the

exploration of the solar system, and select Earth-orbiting missions. The DSN currently consists of three deep-space communication facilities, placed approximately 120° apart around the world, at Goldstone, in California's Mojave Desert; near Madrid, Spain; and near Canberra, Australia. This strategic placement permits constant observation of spacecraft as the Earth rotates, and helps make the DSN the largest and most sensitive scientific telecommunications system in the world.

Over the past years, there has been increasing interest in the use of shorter carrier wavelengths to enhance the DSN's telecommunications and radio science capabilities. Shorter carrier wavelengths, or equivalently higher carrier frequencies, yield greater antenna gains and increased useful bandwidth, with reduced sensitivity to deep-space plasma effects, which tend to degrade the quality of the received signal.

However, there are also new problems associated with the use of higher carrier frequencies, namely greater losses due to gravity-induced antenna deformations and wind, greater sensitivity to misalignments of the radio-frequency (RF) components, and more stringent pointing requirements - all of which are further complicated by time-varying distortions imposed on the antenna structure. Even in the absence of external disturbances, time and elevation dependent loss components are introduced due to the Earth's rotation and the relative motion of the spacecraft as the antenna tracks the target source (whether it is a spacecraft or a radio-source). The combination of these factors can lead to unacceptably large pointing errors and signal-to-noise-ratio (SNR) losses if left uncorrected.

Recovery of SNR losses due to gravitational deformation has been addressed in [1, 2]: here we consider the problem of acquiring and tracking spacecraft with sufficient accuracy to maintain acceptably small losses due to pointing (nominally 0.1 dB) on large DSN antennas.

1.1 The Array Feed Compensation System

A recently developed approach for recovering losses due to gravitational deformations, thermal distortion and wind consists of a real-time compensation system employing a seven-element array of feeds in the focal plane of the antenna's subreflector [1]. The *Array Feed Compensation System* (AFCS) has been evaluated at the DSN's Goldstone complex, and has successfully demonstrated real-time gravity-compensation and closed-loop tracking of spacecraft and radio-source signals at Ka-band frequencies (nominally 32 GHz). Its potential benefits for recovering losses due to mechanical antenna distortions at high frequencies (32 GHz or higher) are described in [2, 3].

A conceptual block diagram of the Ka-band AFCS designed for the DSN's 70-meter antennas is shown in Fig. 1. Its main components are an array of seven 22 dBi horns with a separate Ka-band low-noise amplifier (LNA) connected to each horn; a seven-channel downconverter assembly that converts the 32 GHz RF signal to 300 MHz IF (Intermediate Frequency), followed by a seven-channel baseband downconverter assembly that generates 14 real (seven complex) baseband signals. A digital signal processing assembly then extracts parameters from the digital samples in real-time to obtain the optimum combining weights and determine the antenna pointing updates needed to maximize the combined SNR.

In the absence of antenna distortions, a single properly designed receiving horn collects virtually all of the focused signal power. Distortions generally lead to a shift in the peak of the signal distribution, as well as a redistribution of the signal power in the focal plane. This leads to loss of power in the central channel, which can be effectively recovered by the outer horns of an array placed in the focal plane. When the horn signals are multiplied by complex combining weights matched to the instantaneous magnitude and phase of the signal in each channel, the SNR of the combined channel can be improved, approaching that of an undistorted antenna under ideal conditions.

Distortions also affect the pointing of the antenna by introducing shifts in the signal peak. Antenna pointing errors can degrade the received SNR of both single horn and array receivers, particularly at Ka-band frequencies. We shall demonstrate that properly designed neural network or least-squares algorithms effectively remove the time-varying pointing errors and keep the antenna pointed in the direction of maximum SNR even in the presence of significant antenna distortions.

1.2 Signal Modeling

When the antenna is pointed towards a source such as a distant spacecraft, the “residual carrier” portion of the signal can be filtered out and used to estimate the desired parameters as shown in [2]. The signal in the k -th channel (out of seven) can be represented as

$$r_k(t) = s_k(t) + n_k(t) \quad k = 1, 2, 3, \dots, 7 \quad (1)$$

where the real signal and background noise components are defined as

$$s_k(t) = \sqrt{2}S_k \cos(\omega t + \theta_k) \quad (2)$$

$$n_k(t) = \sqrt{2}[n_{ck}(t) \cos(\omega t) + n_{sk}(t) \sin(\omega t)], \quad (3)$$

where $n_{ck}(t)$ and $n_{sk}(t)$ are uncorrelated baseband random processes representing the in-phase and quadrature components of the noise, and ω represents the Ka-band (32 GHz) carrier frequency. Both the amplitude S_k and phase θ_k of the signal depend on the distortion of the antenna, and also on the pointing offset.

Each channel is downconverted to an intermediate frequency of 300 MHz, after which spacecraft frequency predicts derived from the known spacecraft trajectory are applied and the signals are downconverted to baseband. The resulting complex baseband signals are sampled and “frequency-locked” using a digital frequency-lock loop which eliminates any remaining frequency offsets.

The complex samples so obtained remain essentially constant over time-scales of seconds to minutes, depending on the antenna dynamics, and contain all of the amplitude and phase information used by the tracking and combining algorithms [3]. During actual tracking, sampling rates of 128 per second were typical. These samples can be represented as

$$\tilde{r}_k(i) = \tilde{s}_k(i) + \tilde{n}_k(i) \quad k = 1, 2, 3, \dots, 7 \quad i \in Z \quad (4)$$

where

$$\tilde{s}_k(i) \equiv S_k e^{j\theta_k} \quad (5)$$

with

$$E[\tilde{n}_k(i)] = 0 \quad \text{and} \quad E[\|\tilde{n}_k(i)\|^2] = \text{var}[\tilde{r}_k(i)] = \sigma^2. \quad (6)$$

We assume that noise samples from different channels are independent, as are different noise samples in the same channel. It is convenient to represent the received samples as 7 dimensional complex vectors of the form $\tilde{\mathbf{r}}(i) = \tilde{\mathbf{s}}(i) + \tilde{\mathbf{n}}(i)$, where $\tilde{\mathbf{r}}(i) = (\tilde{r}_1(i), \tilde{r}_2(i), \dots, \tilde{r}_7(i))$ and where each component is defined as in Eq. (5). In order to reduce the effects of noise, the training data set was formed by averaging the received samples over a large number of consecutive received vectors:

$$\tilde{\mathbf{r}}_a(jL) = (\tilde{r}_{a,1}(jL), \tilde{r}_{a,2}(jL), \dots, \tilde{r}_{a,7}(jL)) = \frac{1}{L} \sum_{i=jL-L+1}^{jL} \tilde{\mathbf{r}}(i) \quad j = 1, 2, 3, \dots \quad (7)$$

where

$$\text{var}(\tilde{\mathbf{r}}_{a,k}(jL)) = \frac{\sigma^2}{L}, \quad (8)$$

and $\tilde{\mathbf{r}}_a(jL)$ is the complex averaged vector at time jL – with $\tilde{r}_{a,k}$ referring to its k th complex component – and σ^2 is the variance of the additive white Gaussian noise samples. Thus, with $L = 128$, one-second updates are generated, whereas with $L = 1280$ the effective integration time is 10 seconds. Note that as pointed out above signal amplitudes S_k and phases θ_k are assumed to remain constant over these observations.

1.3 Problem Statement

The instantaneous pointing error vector of the antenna can be represented as (XEL, EL) , a two-dimensional error vector, where XEL is the incremental pointing error in cross-elevation, and EL is the incremental pointing error in elevation measured in millidegrees (mdeg).

We seek to compute the mapping from the 7-dimensional averaged voltage vector $\tilde{\mathbf{r}}_a$ to the two-dimensional error vector (XEL, EL) , as represented by:

$$\begin{bmatrix} XEL \\ EL \end{bmatrix} \leftarrow f(\tilde{\mathbf{r}}_a) \quad (9)$$

Residual errors in the voltage vector \mathbf{r}_a due to noise cause errors in the estimate of (XEL, EL) even if $f(\tilde{\mathbf{r}}_a)$ is known exactly. However, $f(\tilde{\mathbf{r}}_a)$ is also affected by the physical structure of the antenna, which is not always precisely known and which changes as the antenna ages or is buffeted by wind. The noisy and time-varying nature of $f(\tilde{\mathbf{r}}_a)$ poses an additional challenge.

Previous work has demonstrated successful application of interpolated least squares and radial basis function (RBF) networks to correction of antenna pointing errors, based on data from the AFCS, and with the aim of achieving maximum SNR at the horns [4, 5].

Two distinct problems will be considered here: acquisition and tracking. The acquisition problem involves the estimation of antenna-pointing offsets over a wide range. For instance, if the antenna's pointing has drifted by 4 mdeg in XEL and -3 mdeg in EL , an acquisition algorithm must be able to estimate the offset vector $(4, -3)$ accurately in order to re-point the antenna in the correct direction. Otherwise, a severe loss of signal power would result due to the 5 mdeg pointing error magnitude on a 70-meter antenna, which typically has a 9 mdeg beamwidth at 45° elevation.

The second problem, tracking, focuses on significantly smaller offsets. After the antenna has been correctly pointed on source by the acquisition algorithm, it remains necessary to keep it pointed on source to within one millidegree total pointing error despite slow drift in antenna pointing. Accordingly, the tracking

algorithm must estimate small pointing errors near the center of the (XEL, EL) space accurately, and correct them in real-time.

2 Technical Approach

Two approaches, one involving a radial basis function network and the other a quadratic interpolated least squares algorithm, were developed to synthesize the function $f(\tilde{\mathbf{r}}_a)$ described by Eq. (9). Descriptions of both are given below, followed by results and analysis from extensive experiments on real-world and simulated data.

2.1 Radial Basis Function Networks

2.1.1 Training

A radial basis function (RBF) network consisting of a nonlinear radial basis function layer and a linear combiner layer was developed and used to estimate antenna pointing errors [6, 7]. The complex voltage of the center horn was always normalized to $1 + j0$, making it unnecessary to provide this input to the network. This normalization effectively eliminates some of the possible time-dependent variations in the received signal, at the cost of a slight reduction in the total information presented to the algorithms. The network's inputs, therefore, consist of the real and imaginary components of the six normalized horn voltages from the outer horns, for an input vector dimension of 12. In the case of the acquisition networks, a 13th elevation input was also present. The network was trained to generate values for the incremental EL and XEL offsets corresponding to the inputs.

Each radial basis unit implements a Gaussian function of the form

$$G(\tilde{\mathbf{r}}_a(jL); \mathbf{c}_i) = \exp\left(- (b\|\tilde{\mathbf{r}}_a(jL) - \mathbf{c}_i\|)^2\right) = \exp\left(- \left(b \sum_{k=1}^{12} (\tilde{r}_a(jL)_k - c_{ik})^2\right)\right) \quad (10)$$

where $\mathbf{r}_a(jL)$ is the 12-element averaged input voltage vector at time jL (see Eq. (7)), \mathbf{c}_i denotes the i th radial basis center, and $b = 0.8326/\text{spread}$ controls the width of the unit's region of response. The scalar b is defined so that $G(\mathbf{r}_a(jL); \mathbf{c}_i) = 0.5$ when $\|\mathbf{r}_a(jL) - \mathbf{c}_i\| = \text{spread}$.

We define the matrix \mathbf{G} as

$$\mathbf{G} = \begin{bmatrix} G(\tilde{\mathbf{r}}_a(L); \mathbf{c}_1) & G(\tilde{\mathbf{r}}_a(L); \mathbf{c}_2) & \dots & G(\tilde{\mathbf{r}}_a(L); \mathbf{c}_M) & 1 \\ G(\tilde{\mathbf{r}}_a(2L); \mathbf{c}_1) & G(\tilde{\mathbf{r}}_a(2L); \mathbf{c}_2) & \dots & G(\tilde{\mathbf{r}}_a(2L); \mathbf{c}_M) & 1 \\ \vdots & \vdots & \ddots & \vdots & \vdots \\ G(\tilde{\mathbf{r}}_a(NL); \mathbf{c}_1) & G(\tilde{\mathbf{r}}_a(NL); \mathbf{c}_2) & \dots & G(\tilde{\mathbf{r}}_a(NL); \mathbf{c}_M) & 1 \end{bmatrix} \quad (11)$$

where M is the number of radial basis units and N the number of consecutive input voltage vectors applied to the network during the course of operation. The column of ones in \mathbf{G} refers to a bias weight c_{bias} in the linear combiner.

Defining the linear combiner weight matrix as

$$\mathbf{w} = \begin{bmatrix} w_{1,1} & w_{2,1} & \dots & w_{M,1} & c_{bias,1} \\ w_{1,2} & w_{2,2} & \dots & w_{M,2} & c_{bias,2} \end{bmatrix}^T \quad (12)$$

the output of the radial basis network in response to the N input voltage vectors $\mathbf{r}_a(L)$ through $\mathbf{r}_a(NL)$ as computed by the linear combiner becomes:

$$\mathbf{y} = \begin{bmatrix} y_{1,1}(L) & y_{2,1}(2L) & \dots & y_{N,1}(NL) \\ y_{1,2}(L) & y_{2,2}(2L) & \dots & y_{N,2}(NL) \end{bmatrix}^T = \mathbf{w}\mathbf{G} \quad (13)$$

where $y_{j,1}(jL)$ and $y_{j,2}(jL)$ are the RBF network's responses (estimates of EL and XEL) to the j th averaged input vector $\tilde{\mathbf{r}}_a(jL)$ defined in Eq. (7) for $j = 1, 2, 3, \dots$

For acquisition purposes, dual output networks (for EL and XEL) as described above were designed and tested. For the fine tracking case, it was found that best performance with low complexity could be achieved using two single output networks (one for EL and one for XEL).

The number of basis units varies depending on the complexity of the function being approximated and may be quite large in certain cases. In our case, it was determined by the computationally efficient Orthogonal Least Squares (OLS) algorithm described in [7]. This algorithm uses training data points as radial basis function centers, and the weights are obtained as the solution to a least-squares fitting problem.

Differences in the antenna's distortion at different gross elevations led to the training of separate RBF networks for gross elevations of 15, 45, and 75 degrees. The selection of radial basis widths was guided by distances among the voltage vectors in the training set and by experimentation. Since different networks were used for XEL and for EL in the fine tracking case, a total of six networks were designed and evaluated

for tracking. For the coarse acquisition case, estimation of XEL and EL was done by a single network. Only three networks, one for each elevation, were designed for coarse acquisition.

Key network parameters for the fine tracking case, which involved pointing offsets of 2.00 mdeg or less in the XEL and EL directions, are shown in Table 1. Network parameters for coarse acquisition are shown in Table 2.

Tables 1 and 2 show that acquisition requires more radial basis units than fine tracking, since it involves operation over a much larger range in (XEL, EL) space than tracking.

Although it is possible to use larger radial basis spreads to cover the wider area, the function defined in Eq. (9) becomes increasingly complex as we move away from the origin, or “on-source” direction $(0,0)$ in antenna offset space. This rise in complexity in turn makes it difficult to generate good approximations to $f(\mathbf{r}_a)$ without using a large number of units, even if larger radial basis spreads are used.

For instance, at 75° elevation, the acquisition problem requires 77 radial basis units even with the rather large spread of 2.50, while the tracking problem requires only 13 radial basis units (for XEL estimation) to 15 radial basis units (for EL estimation) even with a much smaller spread value. RBF networks for acquisition are not simplified when the XEL and EL estimation problems are separated. The use of separate networks for acquisition merely results in doubling the complexity since each network needs nearly as many basis units as a single network for joint estimation of XEL and EL . The inherent complexity of $f(\mathbf{r}_a)$ over the wider acquisition range thus requires the use of larger, more complex radial basis networks if high accuracy is to be achieved.

2.1.2 Adaptation

In the real world, antenna aging, thermal gradients, and other factors lead to changes in the antenna structure that will change the mapping from the 12-dimensional voltage space to the 2-dimensional (XEL, EL) space. This makes it necessary to continually and incrementally adapt the RBF network mapping to these changes as new data becomes available.

Gradient descent-based learning can be used to adapt all of the parameters of an RBF network including the radial basis spreads and the radial basis centers themselves. While this procedure can adjust all of the network’s parameters over time (except for the number of basis units, which remains fixed), it does not always converge. By contrast, for a *fixed* radial basis layer, it is possible to achieve a global minimum of

the mean-squared error as a function of the linear combiner weights, and good re-training performance is significantly easier to achieve. We take this approach here, and describe below algorithms which avoid the need to generate an entirely new radial basis network using the OLS procedure every time the antenna changes, resulting in computational savings and the ability to adjust the RBF network in near real time.

The LMS Algorithm

Since the linear combiner in the RBF network may be thought of as a linear adaptive filter, the LMS algorithm may be applied to adjust its weights and bias term. Let $\mathbf{x}(n)$ be the input training vector at time n , let $G(\mathbf{x}(n); \mathbf{c}_i)$ denote the output of the i th radial basis unit at time n , $w_i(n)$ denote the corresponding linear combiner weight at time n (the weights are updated on each iteration of the LMS algorithm), and let $c_{bias}(n)$ denote the bias term. The linear combiner calculates

$$y(n) = c_{bias}(n) + \sum_{i=1}^N w_i(n) G(\mathbf{x}(n); \mathbf{c}_i). \quad (14)$$

Updates of the weights are given by

$$w_i(n+1) = w_i(n) + \eta e(n) G(\mathbf{x}(n); \mathbf{c}_i), \quad (15)$$

where $e(n) = d(n) - y(n)$ is the error formed between the desired output $d(n)$ and the actual output $y(n)$. Here η is the learning rate parameter, which can be adaptively updated for faster convergence - see [8]. The bias term is viewed as a weight attached to a fixed input of +1 and updated via

$$c_{bias}(n+1) = c_{bias}(n) + \eta e(n) \quad (16)$$

Pseudo-Inverse Optimization

While the LMS algorithm is a powerful procedure, it is a stochastic approximation to true gradient descent. It is possible to compute the set of linear coefficients for a given training set and fixed radial basis layer which yields the lowest possible mean square error (MSE) [6, 9].

With $\tilde{\mathbf{r}}_j$ denoting the j th training set vector, and \mathbf{c}_i the i th radial basis center, the matrix \mathbf{G} defined by Eq. (11) has a pseudo-inverse given by

$$\mathbf{G}^+ = (\mathbf{G}^T \mathbf{G})^{-1} \mathbf{G}^T. \quad (17)$$

The set of linear combining weights that minimizes the MSE over the training data is

$$\mathbf{w}_{new} = \mathbf{G}^+ \mathbf{d} \quad (18)$$

where \mathbf{d} is the set of desired outputs at times 1 through N defined by:

$$\mathbf{d} = [d(1), d(2), \dots, d(N)]^T \quad (19)$$

Equation (18) always computes the best possible set of weight updates with respect to the mean-squared error criterion over the set of training vectors. The LMS algorithm, by contrast, tends to converge to the optimal weights using stochastic gradient descent, but it does not always reach the best weights. Although it normally comes close to the best weights, the LMS algorithm tends to “hover” in a neighborhood around those weights instead of actually achieving them perfectly.

2.2 Quadratic Interpolated Least Squares

The second approach for approximating the mapping described in Eq. (9) involves use of the quadratic interpolated least squares algorithm.

Consider two vector spaces: a 12-dimensional voltage space and a 2-dimensional (XEL, EL) space. An initial estimate of the antenna pointing offset is obtained by finding the voltage vector in the training (reference) set closest to the observed voltage vector. The corresponding vector in (XEL, EL) space represents our initial estimate of the pointing offset: let us call it $(XEL_{initial}, EL_{initial})$.

Next, the eight closest points to $(XEL_{initial}, EL_{initial})$ in the training set are selected. Using the resulting nine points, one can use one of two methods to obtain the pointing estimates (XEL_{est}, EL_{est}) . The first method uses all eight points and computes a best fit quadratic surface. The coordinates (XEL, EL) where the minimum of this surface occurs, are taken to be the best estimate of the pointing offset. However, it was found that this method offers only a limited advantage over a much simpler quadratic interpolation method, where separate one-dimensional quadratic “slices” were used for XEL and for EL instead of the more complex two-dimensional surface: this simpler method was used in the simulations.

3 Simulation Description

3.1 Simulation of the Antenna with Gravitational Distortion

Spacecraft signals received by the seven-channel AFCS were simulated in two steps. First, a Physical Optics analysis code was used to obtain the electromagnetic field at the focal plane of the antenna where the apertures of the feed horns are located. This code used the 70-m antenna surface-distortion data obtained from holography measurements during the recent holography-cone experiments [3]. The surface distortions were actually measured at 12.7, 37 and 47 degrees elevation and were subsequently interpolated to obtain distortions at other elevations. The resulting distortions were added to the nominal surface data to create the final “distorted” reflector surface data. The field at the feed horns in the focal plane was computed by applying a plane wave incident on the main reflector surface, and by tracing the fields to the focal plane via the sub-reflector.

Next, the computed field data were used to obtain the complex voltages at the horn array, and the field and power over the aperture of each individual horn was determined. The difference between the power captured by the feed horns and the total power at the focal plane is an indication of feed array efficiency. In a separate calculation, the fields at the aperture of each horn, induced by the application of a unit voltage to the input of the horn, were calculated using a theoretical waveguide modal expansion. These fields were subsequently convolved with the received focal plane fields at the aperture of each horn in order to calculate the final complex voltage. Details of these calculations are omitted here for space considerations.

Figures 2 through 4 show the normalized received power distribution on the focal plane of the reflector at 15°, 45°, and 75° elevations, respectively. The feed apertures of the array are superimposed on the plots to indicate the power distribution captured by each horn. It can be seen that at 45° where the reflector surface is designed to provide “optimal” performance, most of the energy is captured by the center horn. On the other hand, at 15° and 75° elevations, where the effects of gravitational distortions are significant, considerable energy falls beyond the center horn but is largely recovered by the ring of array elements. As can be seen, the effects of distortions are particularly pronounced at 75° elevation angle. Figure 3 shows that even in the presence of the surrounding feed elements some of the energy falls between the horns and therefore is not fully recovered. However, simulations also show that the surrounding ring elements can be rotated to a position that increases the captured power by more than 0.5 dB. Furthermore, an additional 1 dB

in efficiency can be obtained by optimally repositioning the entire array in the focal plane, or equivalently repointing the antenna in the direction that yields maximum combined SNR.

3.2 Tracking Regions

Although the test sets for tracking were defined over a finely spaced grid ranging from -2.00 mdeg to $+2.00$ mdeg in both XEL and EL , it is still useful to evaluate the algorithms' performance over varying ranges in (XEL, EL) space since, for example, one algorithm may yield better performance very close to the "on-source" direction $(0, 0)$ while another may yield better performance over a greater range of pointing offsets. The tracking regions for the simulations are defined in Table 3. Error statistics were generated for each of the five tracking regions to illustrate possible performance differences between the RBF network and the quadratic interpolated least squares algorithm.

3.3 Simulating Changes in the Antenna Structure

Both acquisition and tracking performance can be adversely affected by changes in the antenna structure, in which case it becomes necessary for the radial basis networks to adapt to such changes. This is particularly important for fine tracking algorithms since they are responsible for keeping the antenna pointed accurately on source throughout the track.

Changes in the antenna structure were simulated by altering the mapping from voltage space to (XEL, EL) space when generating the training sets for the RBF networks. Let the mapping from voltage space to offset space be given by Eq. (9), and create a distorted mapping by changing the (XEL, EL) values corresponding to the voltage vectors using, for example, the following equations:

$$XEL_{old} = \frac{3}{4}XEL_{new} + \frac{1}{2}mdeg \quad (20)$$

$$EL_{old} = \frac{5}{4}EL_{new} + \frac{1}{2}mdeg \quad (21)$$

One may think of XEL_{old} and EL_{old} as being the correct offsets corresponding to given voltage vectors for the antenna at time t_1 . Antenna aging and other factors may cause the same voltage vectors to map to XEL_{new} and EL_{new} at time t_2 , where we have assumed t_1 and t_2 to be far apart since the idea is to model

long-term changes. The RBF networks were trained on the old data in an effort to generate a set of distorted mappings. We can say that these training data were correct at time t_1 in the distant past but changes in the antenna have yielded a new mapping at time t_2 . We seek to update the RBF network parameters so the networks will accurately determine offsets under the new mapping according to the adaptation strategies discussed in Section 2.1.2.

4 Simulation Results

4.1 Acquisition Performance Comparison

Figures 5 and 6 illustrate the mean error and error standard deviation (or RMS error) of the radial basis network and the interpolated least squares algorithm at 45° of antenna elevation with 10-second integration. In these figures, both the mean errors and error standard deviations have been averaged over the entire “acquisition range”. The error in XEL and the error in EL were calculated for each of these grid points. The mean acquisition error in each variable (in XEL and in EL) and the RMS error in each variable were then computed over the entire acquisition test grid.

One can compute an instantaneous estimate of pointing offset using a single voltage vector sample. This technique corresponds to 1-second averaging, assuming the system is updated at a rate of one sample per second. We can also compute 10-second averages in which the input voltage vector is averaged over a period of 10 seconds. The 10-second averaging scheme results in averaged samples which exhibit a lower variance than unaveraged 1-second samples. Both techniques were tested for acquisition purposes.

For radial basis networks, mean errors with 10-second averaging were found to be typically less than 0.1 millidegree for SNR above 20 dB-Hz, as illustrated by Fig. 5, which is representative of results achieved at other elevations. It should be noted that a 10 dB improvement in SNR is associated with 10-second integration, resulting in smaller mean errors. The choice of integration period (10 seconds) is quite realistic and is dictated by the antenna’s mechanical system which cannot respond to faster, 1-second updates.

Figure 6 illustrates the error standard deviation of both the RBF network and the quadratic least-squares algorithm with 10-second integration. The results shown in this figure are representative of those achieved at other elevations. At high SNR the quadratic least squares algorithm’s performance does not improve with increasing SNR as expected, but tends to approach an RMS “error floor” of a few tenths of a millidegree.

This irreducible error appears to be due to decreased accuracy of the interpolation algorithms near the outer edges of the acquisition range, where simple approximations to the error surface tend to break down. For medium to high SNR (greater than 20 dB-Hz), the radial basis network outperforms the least squares algorithm in acquisition mode, whereas in the low SNR region from 10 dB-Hz to approximately 15 dB-Hz the least squares algorithm yields best performance. These results suggest the use of a hybrid system consisting of a least squares algorithm for low SNR acquisition, and a radial basis function network for the medium to high SNR regions.

In summary, these simulations have demonstrated that the RBF neural network yields better mean error and RMS error performance in the medium to high SNR range during acquisition. However, under very noisy conditions in acquisition mode the quadratic interpolated least squares algorithm yields the lowest RMS and mean errors; hence, this algorithm is preferred in the low SNR regions.

4.2 Tracking Performance Comparison

Tracking involves estimation and correction of small pointing errors. Tracking algorithms need only be optimized for accurate estimation of errors over a small range: our tests were performed by applying offsets ranging from -2.00 mdeg to 2.00 mdeg in both XEL and EL .

As previously discussed, five tracking regions were defined for evaluation purposes. The first region was really the point $(0,0)$ in (XEL, EL) space, where the mean error and error standard deviations of the estimates were determined with the antenna simulated pointing perfectly on source in the presence of noise. The next region is a square centered at $(0,0)$, and the remaining regions are progressively larger squares, as defined in Table 3.

4.2.1 RBF Network Performance

Figures 7 through 9 show the desired target points in (XEL, EL) space denoted by dark “x” symbols and the estimates computed by the RBF networks as light dots. For each offset, shown as a dark “x”; 100 independent estimates from the RBF network were used to obtain a scatter plot of the neural networks’ estimates of the applied antenna offsets. These light dots form clusters near the target points, and the size and the center of each cluster give a rough indication of neural network performance.

Each scatter plot was taken at an SNR of 40 dB-Hz with 10-second integration, illustrating performance

over region 3 as defined in Table 3. It is interesting to observe that performance is better at low and high elevations, where there is significant antenna distortion, than at 45° elevation where distortion is minimal. This is attributed to the fact that more signal power is present in the outer horns when there is distortion, providing more information to the RBF network for a better estimate of the applied offset. However, we also observe a slight bias at 75° of elevation, evidenced by the fact that the clusters of estimates (light dots) are not centered perfectly on the true offsets (dark “x” symbols). A summary of RBF network performance in terms of mean error and error standard deviation at 40 dB-Hz SNR, with 10-second integration, is provided in Table 4.

4.2.2 Least Squares Performance

A scatter plot for the quadratic interpolated least squares algorithm is given in Fig. 10. At 75° elevation estimator bias starts to become significant. The error standard deviation and mean error of the least squares algorithm, averaged over the entire grid, are shown in Table 5.

4.2.3 Performance Comparison

The least squares algorithm evaluated here implicitly assumes a quadratic error surface since it uses quadratic interpolation. This assumption appears to be good at both 15 and 45 degrees elevation where performance is nearly identical to that of the RBF networks.

At 75° elevation, the antenna surface suffers significant distortion. The spatial distribution of power in the focal plane is greatly affected by these distortions, and a significant amount of power appears in the outer horns. Furthermore, the assumption of a quadratic error surface only appears to hold for a very small neighborhood in this region, with a breakdown of the quadratic assumption becoming evident as we move away from (0,0) in antenna offset space as shown in Fig. 10.

The RBF network is better able to deal with severe antenna distortion as illustrated in Fig. 9. Under the high SNR conditions shown in Figs. 9 and 10, the clusters are very small for both algorithms at 75° elevation. The errors in the least squares algorithm at this elevation are mostly *systematic* with very little random error, indicating breakdown of the quadratic surface assumption at high elevations when the antenna’s main reflector is severely distorted.

Figures 11 through 18, which highlight performance over region 3, defined over ± 1.00 mdeg in antenna

offset space, are representative of results achieved for all five regions. Figures 11 through 14 show the mean errors obtained with both the interpolated least squares and RBF network algorithms. Both one-second and ten-second integration times are included in the error plots. Error standard deviations are illustrated in Figs. 15 through 18. In all cases, errors in millidegrees are plotted against SNR in dB-Hz.

RBF networks generally exhibit higher mean errors at low SNR than the least squares algorithm. At medium-to-high SNR the RBF network’s performance does not differ significantly in terms of mean error. Furthermore, the error standard deviations are comparable, indicating the RBF network comes close to the performance of the quadratic interpolated least squares algorithm without significant differences in random error.

For 75° of elevation, the RBF network exhibits an advantage in terms of overall performance, mostly due to its ability to better handle non-quadratic error surfaces which are characteristic of severely distorted antennas.

Overall, both algorithms exhibit similar performance for tracking at elevations of 15 and 45 degrees, while the RBF network performs better than the quadratic interpolated least squares algorithm at very high elevations corresponding to severe antenna distortion.

We observe that both algorithms achieve the nominal 0.8 mdeg total pointing accuracy requirement at SNR above approximately 20 dB-Hz at all elevations when 10-second integration is used. This integration time is compatible with the practical update rate of the antenna and represents outstanding “weak signal” performance. Even with 1-second integration both algorithms meet the 0.8 mdeg requirement above 30 dB-Hz, although pointing corrections generally cannot be applied to the antenna at such a high rate.

4.3 Adaptive Tracking Results

As discussed in Section 3.3, a simple affine transform was used to simulate a changed antenna and to determine the performance of the radial basis network on translational, shrink, and stretch distortions. Six RBF networks were trained on voltage-to-offset mappings representing the antenna in the “old” state. The affine transform was used to change the voltage-to-offset mapping, and the RBF networks were simulated on the “new” antenna state both before and after undergoing re-training.

In Fig. 19 (40 dB-Hz and 10-second integration times) we see that the estimates (red clusters) corresponding to the antenna offsets from the RBF networks are very far from the dark “x” symbols denoting the

new values. This illustrates the performance of the networks trained on old data representing, for example, a pointing bias and scaling due to aging. Our objective is to re-train the networks to remove the pointing bias by adapting their linear combiners.

For the 75° elevation case, Fig. 20 shows the error standard deviations, which indicate an “error floor” of about 0.2 mdeg even at high SNR. There is also a systematic pointing error of -0.5 mdeg in both coordinates resulting from training on the old data which dominates the mean error.

4.3.1 LMS Results

Using an updated set of training data, the RBF networks were re-trained using the LMS algorithm. The resulting networks, with 10-second integration and an SNR of 40 dB-Hz, yield the performance illustrated in Fig. 21, which is representative of results achieved at other elevations. Much of the systematic pointing bias has been successfully removed.

The error standard deviation is also shown as a function of SNR for the 75° case in Fig. 22, illustrating significant improvements due to adaptation. After LMS retraining the network achieves significantly improved performance, although it does not achieve the same performance as a network created using the new data and the OLS algorithm. While the pointing biases have been successfully removed, we see from figure 21 that the distortion has not been fully eliminated. This is due to several factors. The number of radial basis units, along with their centers and their widths, remained fixed in this adaptation approach. It is likely that the optimal set of centers for the old data is not the optimal set of centers for the new data. Furthermore, LMS is a stochastic gradient descent procedure which does not implement true, noiseless gradient descent; hence, there is some noise in the convergence process. The performance improvements after adaptation are nonetheless dramatic and important.

4.3.2 Pseudo-Inverse Optimization

As shown in Figs. 23, the pseudo-inverse method yields superior training performance, with most of the error caused by the old training set well-corrected after re-training is complete. As with the LMS case, the results obtained at 75° are representative of results obtained at other elevations. The LMS method also yields acceptable performance, but LMS is a stochastic gradient descent procedure. It is therefore only an approximation to the true gradient descent algorithm, and even true gradient descent takes many iterations to

converge asymptotically to the optimal weight vector \mathbf{w} . By contrast, the pseudo-inverse method calculates a set of weights which yields the lowest possible MSE for a fixed radial basis layer [6, 9].

If near real-time updating is desired, it may be advisable to use the LMS algorithm, although storing and averaging data to form new training sets to update the linear combiner weights using the pseudo-inverse method would likely yield better performance. While it is possible to use the OLS method to re-generate the RBF neural networks, such re-generation is the most computationally expensive option and is not recommended unless significant changes in the antenna have occurred.

5 Real-World Experimental Data Results

Data collected during observations of the DS1 spacecraft¹, as described in [4], were also used to evaluate the RBF network. Since antenna distortion is elevation-dependent, data were collected at virtually all elevations from less than 10° (near the horizon) to over 80° (close to zenith). The data were grouped in elevation bands spanning 0-10 degrees elevation, 10-20 degrees, and so on, up to the highest band covering 80-90 degrees. The signal source was the 32 GHz residual carrier of the spacecraft DS1, which was in cruise mode near the earth, providing a strong and stable signal.

While tracking the residual carrier, the antenna pointing was refined by means of a “five-point boresighting” algorithm that introduced ± 4 mdeg pointing offsets in two orthogonal directions along the line-of-sight. The algorithm then measured the signal power in the central horn (channel 1) at each offset as well as with no offset (nominal on-source direction) and computed a pointing update based on a quadratic fit to the data. After a few iterations, the magnitude of the updates approached zero, and the signal power in the central channel was maximized: this was considered to be the true “on-source” direction. The antenna was allowed to track the source using its own tracking model which takes into account both the rotation of the earth and the relative motion of the spacecraft.

Following this fine-pointing operation, a raster-scan was initiated. The antenna was commanded to predetermined offsets from the nominal on-source direction, and the received vector measured at each point. The raster-scan consisted of the offsets (in mdeg) 0, ± 2 , ± 4 , ± 6 in both the elevation and cross-elevation directions (these refer to local orthogonal coordinates defined around the line-of-sight). Note that the zero-offset case defines the effect of antenna distortions on the received complex signals at that elevation, whereas

the other cases contain a mixture of both distortion and pointing effects. In order to remove some possible time-dependent variations in the data, the data vectors were normalized by the complex value of the central horn (channel 1), so that the real and imaginary parts of first component were always 1 and 0, respectively. Thus, only the response of the six outer horns were used to train the network.

5.1 Performance Evaluation

After the RBF network was trained with the averaged training data-set, its performance on tracking data obtained on days 29 and 38 was evaluated. Although some of the DS1 raster scan data used for performance evaluation from these two days also contributed to the training data-set (along with raster scan data from several other tracks), there was no noticeable change in performance when compared to tracking segments that were not averaged into the training-set, such as five-point boresights. Table 6 highlights the performance obtained with our two data sets.

As expected, performance was found to be a strong function of SNR. For very low SNR, mean errors and error standard deviations could exceed 1 millidegree. For high SNR cases, errors were typically less than 0.5 millidegrees, which is significantly better than the nominal 0.8 mdeg pointing accuracy requirement for Ka-band communications on the 70-meter deep space antenna.

Figures 25 and 26 illustrate the ability of the neural network to estimate the incremental pointing offsets applied to the antenna as it tracked the source. The light gray lines indicate the incremental pointing offsets applied in either the *EL* or *XEL* directions, while the dark, thin lines indicate the radial basis network's estimate of the applied pointing offset. The error in estimating the antenna pointing offset is the vertical distance between the two. These two lines are generally very close, highlighting the radial basis network's ability to estimate pointing offsets accurately in this region.

Additional observations can be made from the two plots in Figs. 25 and 26. First, even with one second integration tracking is generally very good with only slight errors, typically well under 1 millidegree. Second, note that in typical applications the noisy output of the radial basis network can be further improved by averaging, thus achieving even better performance. Such averaging was not performed here due to the rapid changes in the artificially applied offsets, such as the ± 4 millidegree spikes (boresights). During actual tracking under calm conditions, longer integrations (or averaging of several one-second integrations) would be performed to improve the estimates: thus, with 4 second integration (or averaging of 4 one-second

voltage input vectors) the standard deviation of the estimates is reduced by a factor of two, with 9 seconds a factor of 3, and so on.

Occasional error spikes can also be observed in these plots. These are generated by large changes in the “other” variable. This effect is the result of cross-coupling between the *XEL* and *EL* directions, due to a slight (approximately 10 degree) rotation of the feed array axes with respect to the antenna axes due to physical constraints on the antenna. For example, the sharp drop in the radial basis network’s estimate of *XEL* just after 25 seconds and also near 170 seconds in Fig. 25 corresponds to a sudden 4 mdeg change in *EL* occurring at the same time. However, in an operational system, cross-coupling will be minimized by careful alignment; hence, this effect is not expected to be significant. In addition, since the cross-coupling effect appears as a sudden change in the mean of the estimate, averaging several one-second estimates (as is the case in real-world operation) tends to reduce this effect proportional to the number of measurements averaged. Thus, if cross-coupling affects a single one-second estimate then averaging 4 measurements will tend to reduce it by a factor of 4, and so on. However, even with the cross-coupling errors included in the calculation of the sample-variance, the resulting standard deviation of estimation error remains under 0.5 millidegrees in both the *XEL* and *EL* directions in this region.

6 Conclusions

We have shown that both interpolated least squares and adaptive RBF networks, working in conjunction with an array feed compensation system, can point a 70-meter deep space antenna with RMS errors of 0.1-0.5 millidegree, under a wide range of signal-to-noise-ratios and antenna elevations, achieving significantly higher accuracies than the 0.8 millidegree benchmark for communications at Ka-band frequencies of 32 GHz.

As such they demonstrate clear potential for highly accurate pointing of the 70-meter DSN antennas, which is an extremely challenging problem due to a multitude of time-varying distortions imposed on the antenna structure on a continuous basis.

Results indicate that RBF networks perform as well or better than quadratic interpolated least squares algorithms at varying antenna elevations for tracking and acquisition, and under a wide range of SNR conditions. At high antenna elevations, the quadratic interpolation method deteriorates for any significant offset

from the “on-source” direction, making RBF networks especially attractive during high elevation operations.

Long-term adaptation of our algorithms for distorted antennas has also been shown to result in significantly improved performance. We have shown that adaptation of the linear combiner weights in the RBF network yields excellent performance for simple stretch, shrink, and translational distortions.

The system described in this paper is currently in testing phases at NASA’s Goldstone DSN station, and slated for implementation for real-time, adaptive acquisition and tracking of the antenna, marking the first real example of a computationally intelligent telecommunication application for NASA’s deep space network.

References

- [1] V.A. Vilnrotter, E.R. Rodemich, and S.J. Dolinar Jr., “Real-time combining of residual carrier array signals using ML weight estimates,” *IEEE Trans. Communications*, vol. 40, pp. 604–615, March 1992.
- [2] V.A. Vilnrotter, “Channel assignments for improved gain in baseband array feed compensation systems,” *IEEE Trans. Communications*, vol. 42, pp. 2127–2133, May 1994
- [3] V. Vilnrotter and D. Fort, “Demonstration and Evaluation of the Ka-Band Array Feed Compensation System on the 70-Meter Antenna at DSS 14,” *Telecommunications & Mission Operations Progress Report 42-139*, JPL, Pasadena, CA, Nov. 15, 1999, <http://tmo.jpl.nasa.gov/>
- [4] R. Mukai, P. Arabshahi, and V. Vilnrotter, “An array feed radial basis function tracking system for NASA’s deep space network Antennas,” *Proc. International Joint Conference on Neural Networks*, July 24–27, 2000.
- [5] R. Mukai, V. Vilnrotter, P. Arabshahi, and V. Jamnejad, “Computationally intelligent array feed tracking algorithms for large DSN antennas,” *Telecommunications & Mission Operations Progress Report 42-141*, JPL, Pasadena, CA, May 15, 2000, <http://tmo.jpl.nasa.gov/>
- [6] Simon Haykin, *Neural networks: a comprehensive foundation*, Prentice Hall, 1998.

Gross EL (deg)	Radial Basis Spread	Variable Estimated	Number of Basis Units (M)
15	0.6250	<i>XEL</i>	6
15	0.6250	<i>EL</i>	3
45	0.7500	<i>XEL</i>	6
45	0.7500	<i>EL</i>	8
75	0.7500	<i>XEL</i>	13
75	0.7500	<i>EL</i>	15

Table 1: Radial Basis Neural Network Parameters for Tracking Networks

Gross EL (deg)	Radial Basis Spread	Variable Estimated	Number of Basis Units (M)
15	0.50	<i>XEL</i> and <i>EL</i>	127
45	0.70	<i>XEL</i> and <i>EL</i>	103
75	2.50	<i>XEL</i> and <i>EL</i>	77

Table 2: Radial Basis Neural Network Parameters for Acquisition Networks

- [7] S. Chen, C.F.N. Cowan, and P.M. Grant, “Orthogonal least squares learning algorithm for radial basis function networks,” *IEEE Transactions on Neural Networks*, vol. 2, no. 2, pp. 302–309, March 1999.
- [8] P. Arabshahi, J.J. Choi, R.J. Marks II, and T.P. Caudell, “Fuzzy parameter adaptation in optimization: some neural net training examples,” *IEEE Computational Science and Engineering*, vol. 3, no. 1, pp. 57–65, Spring 1996.
- [9] C.L. Lawson and R.J. Hanson, *Solving least squares problems*, Society for Industrial and Applied Mathematics, Philadelphia, 1995.
- [10] The Deep Space One Mission, *Jet Propulsion Laboratory*, <http://nmp.jpl.nasa.gov/ds1/>

Region 1	(0,0)
Region 2	Square. ± 0.50 mdeg in <i>XEL</i> and in <i>EL</i> .
Region 3	Square. ± 1.00 mdeg in <i>XEL</i> and in <i>EL</i> .
Region 4	Square. ± 1.50 mdeg in <i>XEL</i> and in <i>EL</i> .
Region 5	Square. ± 2.00 mdeg in <i>XEL</i> and in <i>EL</i> .

Table 3: Test Regions for Tracking Performance Evaluation

Elevation	Variable	Mean Error (mdeg)	Error Standard Deviation (mdeg)
15 deg	<i>XEL</i>	-0.0005	0.0491
15 deg	<i>EL</i>	0.0434	0.0350
45 deg	<i>XEL</i>	0.0009	0.0696
45 deg	<i>EL</i>	0.0231	0.0523
75 deg	<i>XEL</i>	0.0052	0.0380
75 deg	<i>EL</i>	0.0090	0.0258

Table 4: RBF Network Tracking Performance at 40 dB-Hz with 10-second integration

Elevation	Variable	Mean Error (mdeg)	Error Standard Deviation (mdeg)
15 deg	<i>XEL</i>	0.0008	0.0437
15 deg	<i>EL</i>	0.0154	0.0330
45 deg	<i>XEL</i>	0.0001	0.0685
45 deg	<i>EL</i>	0.0034	0.0633
75 deg	<i>XEL</i>	0.0000	0.0819
75 deg	<i>EL</i>	0.0268	0.0422

Table 5: Quadratic Interpolated Least Squares Performance at 40 dB-Hz with 10-second integration

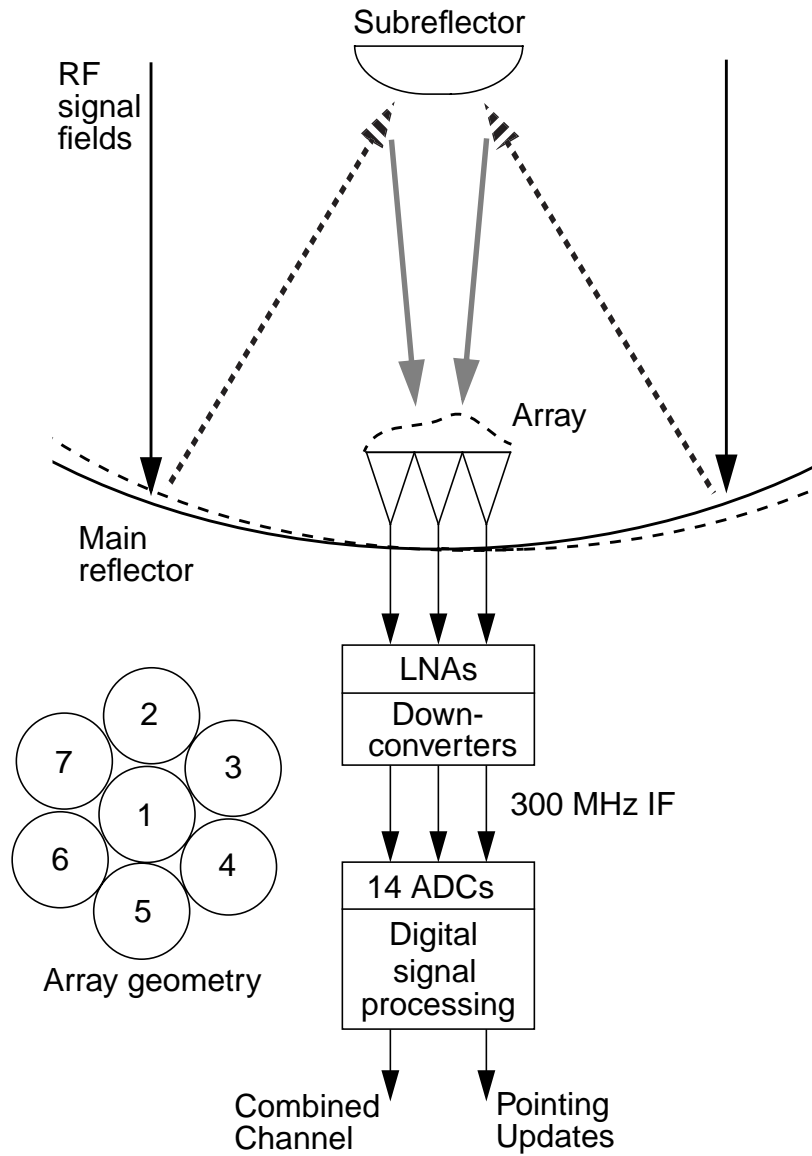


Figure 1: Conceptual block diagram of array feed compensation-tracking system

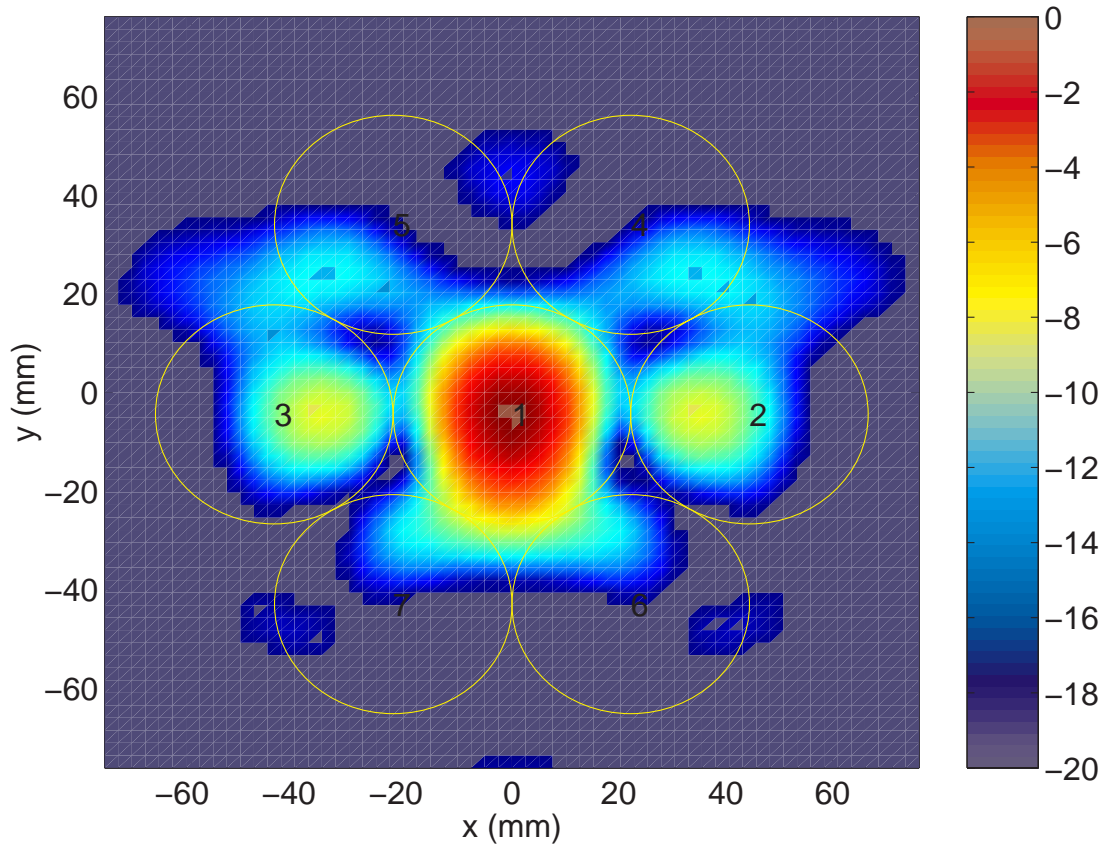


Figure 2: Normalized received power distribution (dB) on focal plane of 70-meter reflector. Elevation: 15°

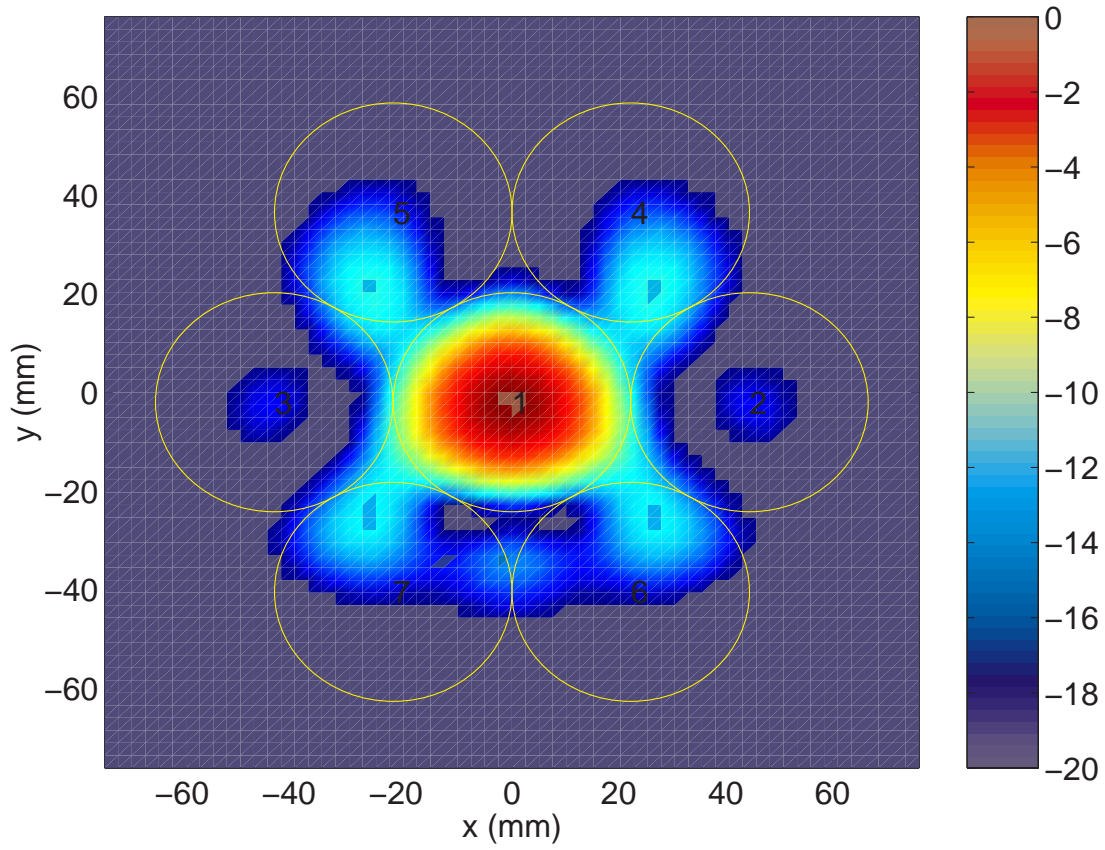


Figure 3: Normalized received power distribution (dB) on focal plane of 70-meter reflector. Elevation: 45°

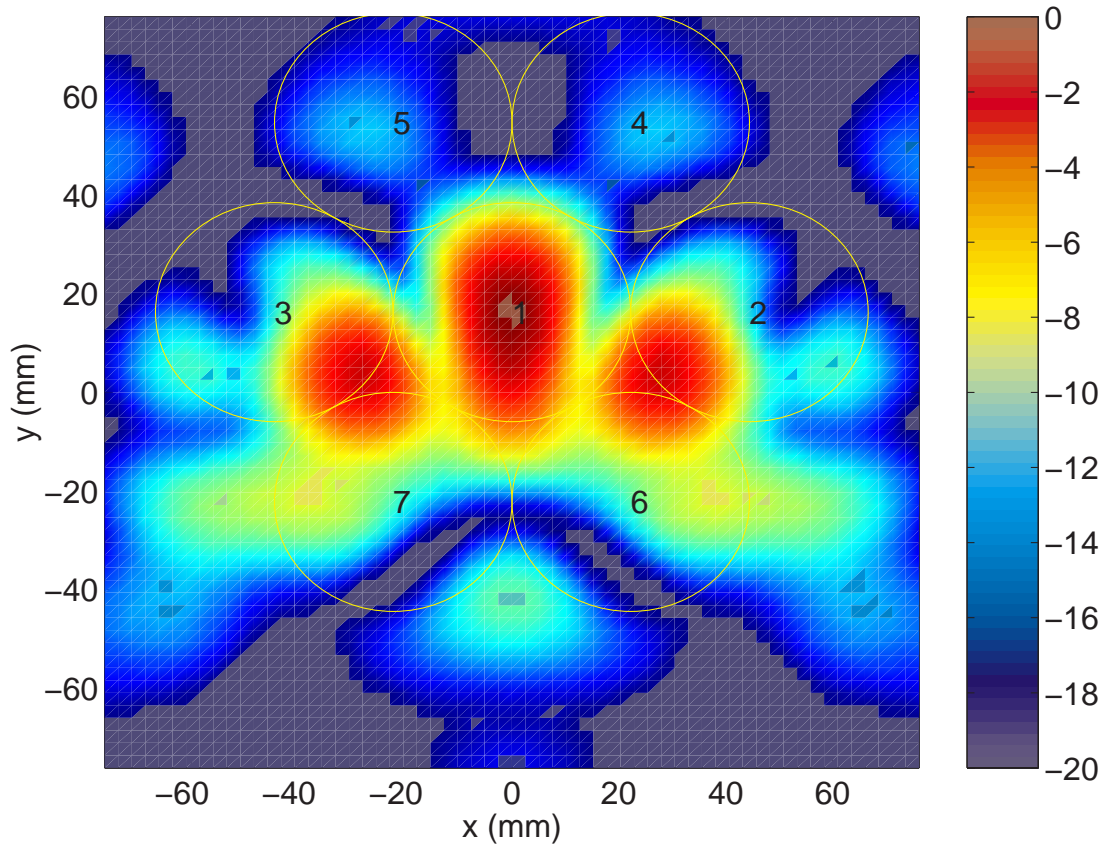


Figure 4: Normalized received power distribution (dB) on focal plane of 70-meter reflector. Elevation: 75°

Day/ Region	Gross Elevation (deg)	Gross Azimuth (deg)	e_{XEL} (mdeg)	s_{XEL} (mdeg)	e_{EL} (mdeg)	s_{EL} (mdeg)	SNR (dB-Hz)	Direction of Gross EL
29/1	57.4-64.7	96.9-104.7	-0.0505	0.4207	0.0507	0.4147	30 to 40	Rising
29/1	57.4-64.7	96.9-104.7	0.1501	0.3152	-0.0204	0.2708	> 40	Rising
29/3	61.1-65.0	254.4-259.1	0.1318	0.4112	0.0419	0.4153	30 to 40	Rising
29/4	55.1-59.9	260.4-264.8	0.1262	0.6722	-0.1662	0.5116	30 to 40	Rising
29/4	55.1-59.9	260.4-264.8	0.2267	0.3488	-0.1797	0.3249	> 40	Rising
38/1	69.3-72.7	113.8-122.0	-0.1985	0.7383	0.0454	0.9468	20 to 30	Rising
38/4	77.3-79.6	142.0-191.9	-0.2711	0.6834	0.2703	0.6941	20 to 30	Rising
38/4	77.3-79.6	142.0-191.9	-1.1917	1.4167	-0.2350	1.1166	10 to 20	Rising

Table 6: Mean elevation and cross-elevation error (e_{XEL}, e_{EL}); corresponding standard deviations (s_{XEL}, s_{EL}), for test data on different regions of days 29 and 38; and corresponding gross elevation/azimuth, and SNR

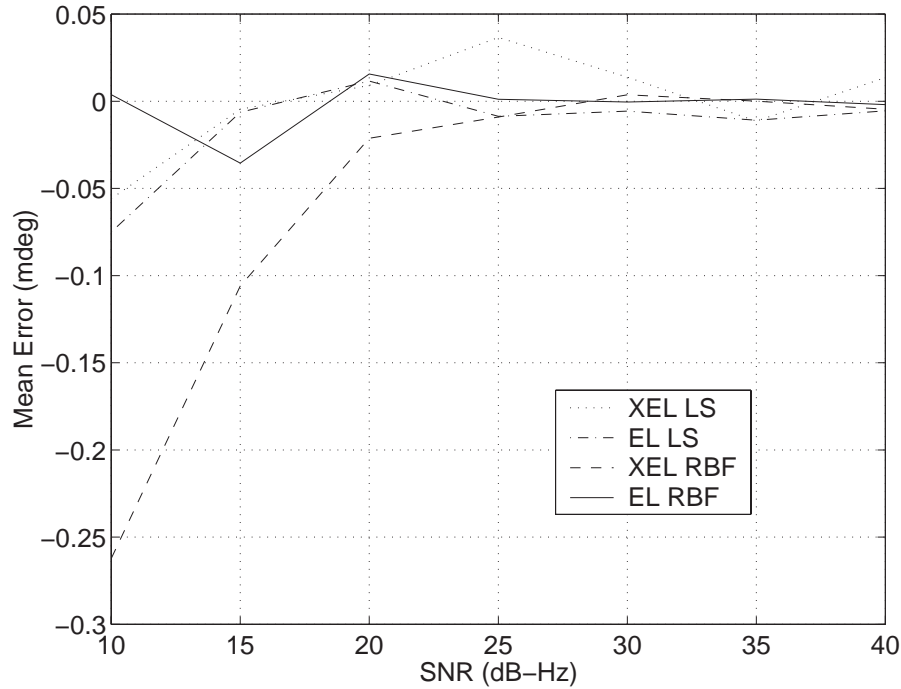


Figure 5: Average offset estimation errors as a function of SNR for both RBF network and interpolated least squares algorithms at 45° elevation with 10-second integration

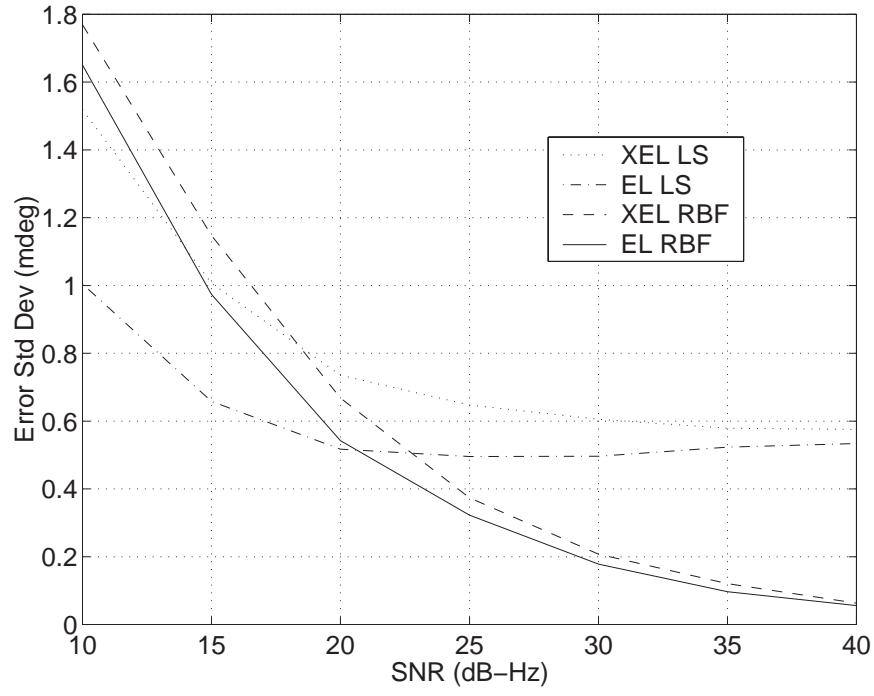


Figure 6: Error standard deviations as a function of SNR for both RBF network and interpolated least squares algorithms at 45° elevation with 1-second integration

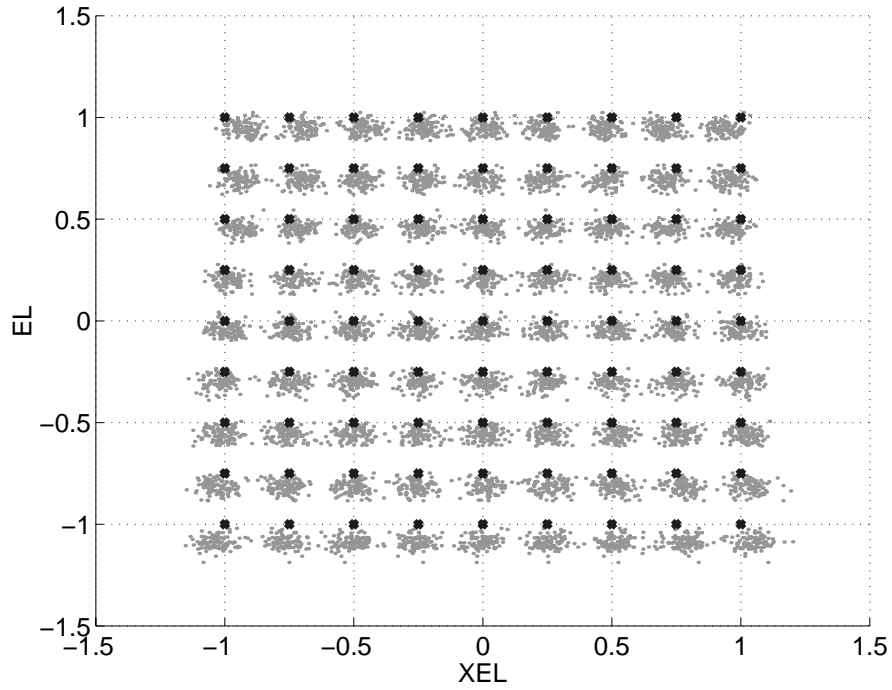


Figure 7: RBF Region 3: 15° , 40 dB-Hz, 10-second integration

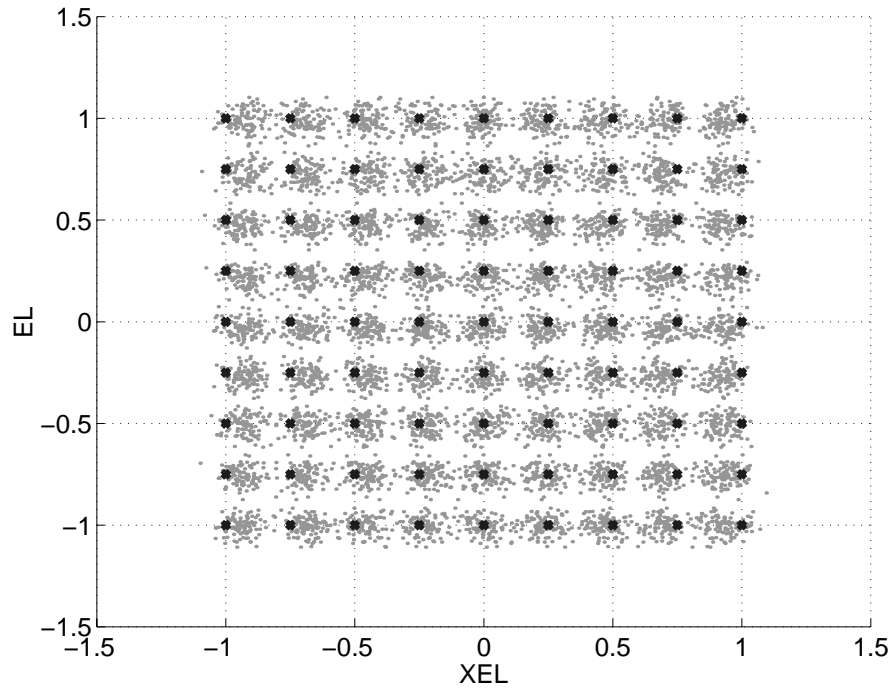


Figure 8: RBF Region 3: 45° , 40 dB-Hz, 10-second integration

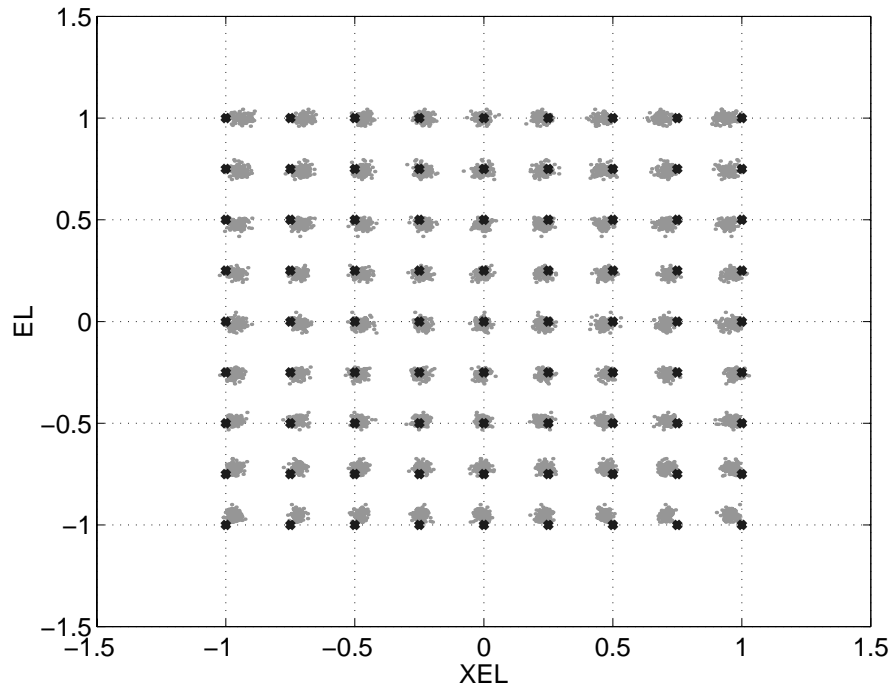


Figure 9: RBF Region 3: 75° , 40 dB-Hz, 10-second integration

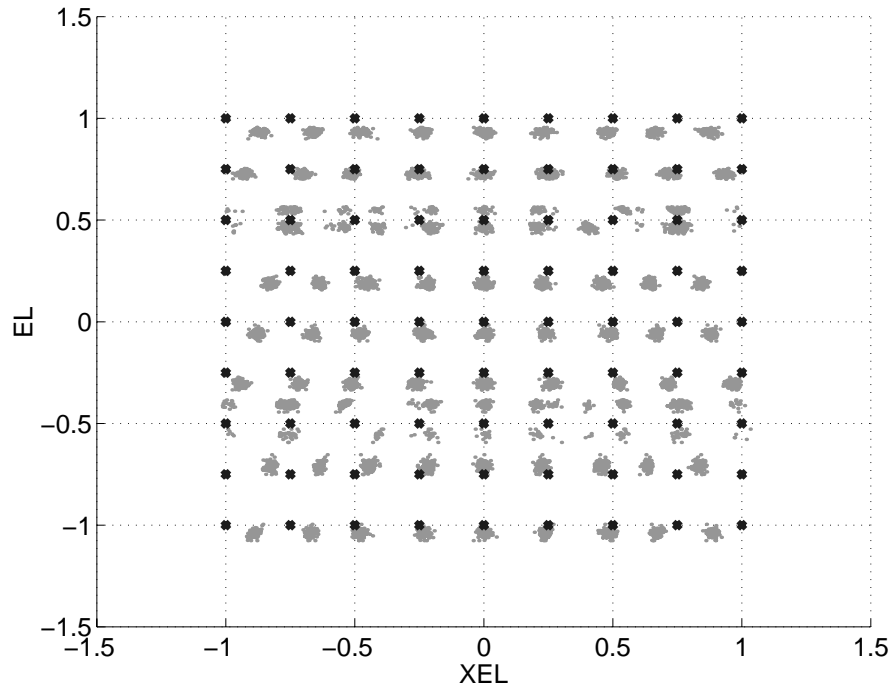


Figure 10: LS Region 3: 75° , 40 dB-Hz, 10-second integration

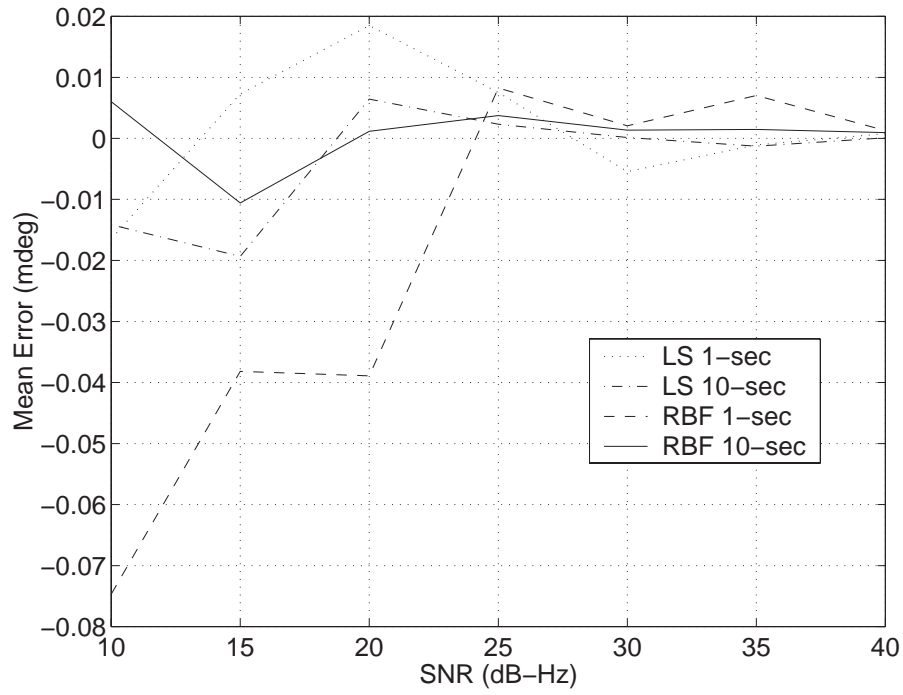


Figure 11: Mean errors $XEL 45^\circ$

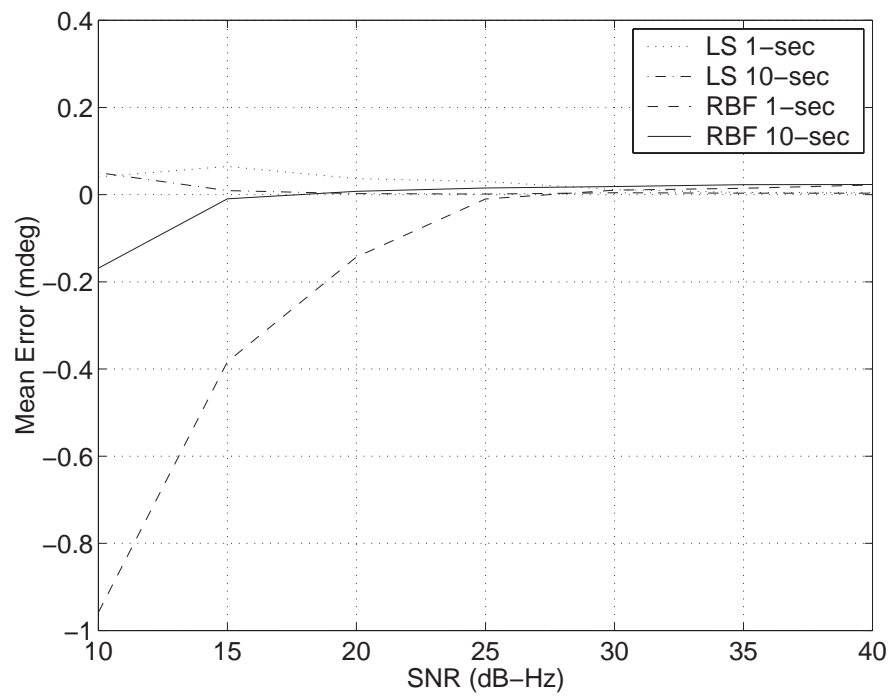


Figure 12: Mean errors $EL\ 45^\circ$

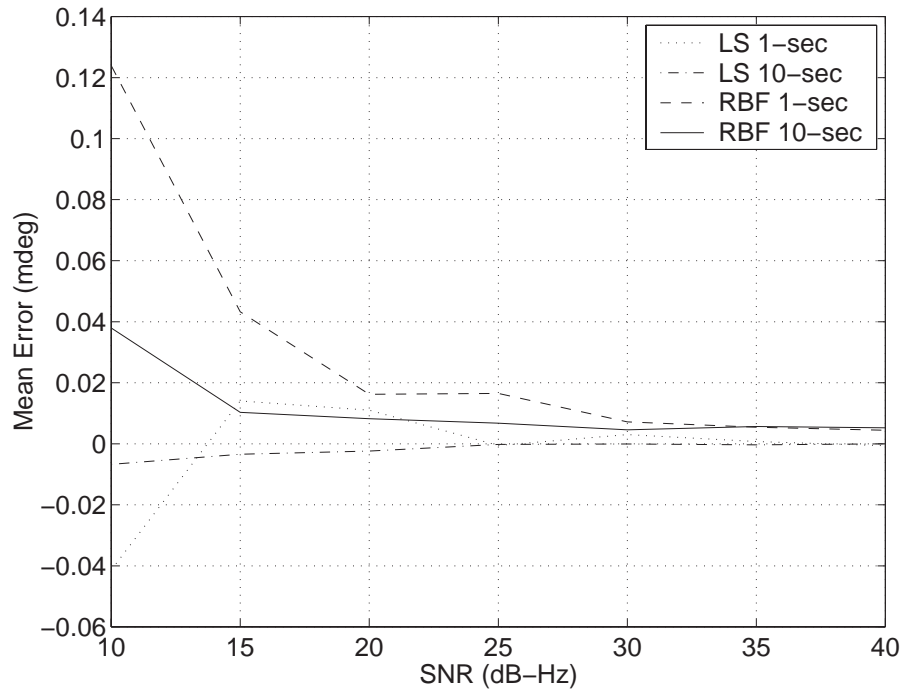


Figure 13: Mean errors $XEL\ 75^\circ$

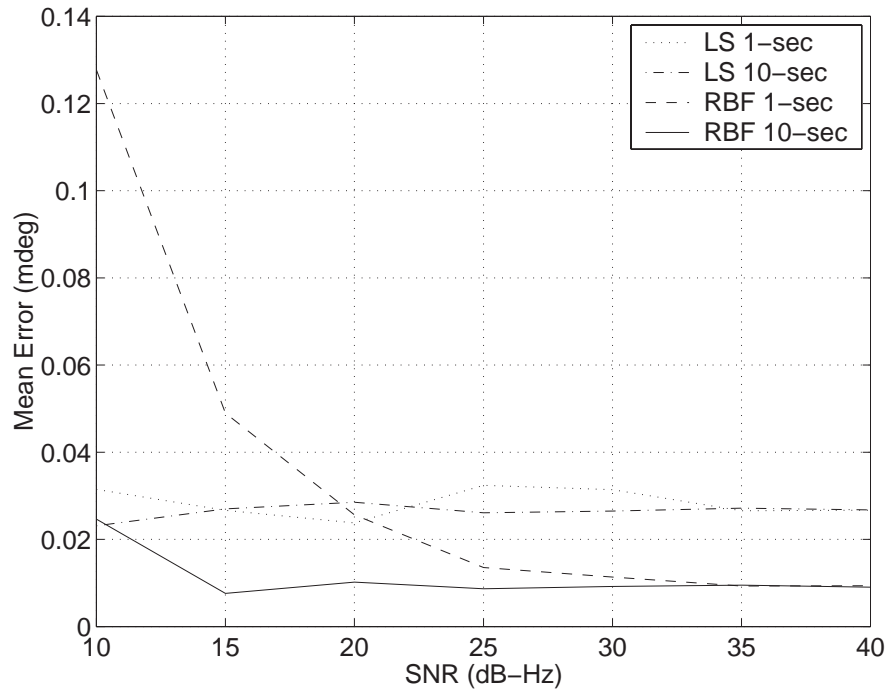


Figure 14: Mean errors $EL\ 75^\circ$

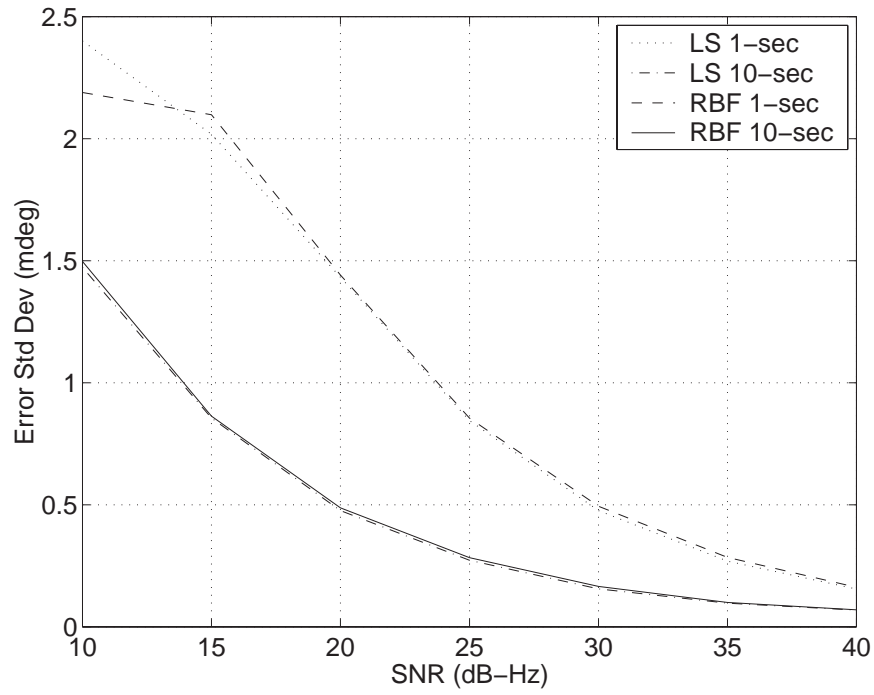


Figure 15: Error standard deviations $XEL\ 45^\circ$

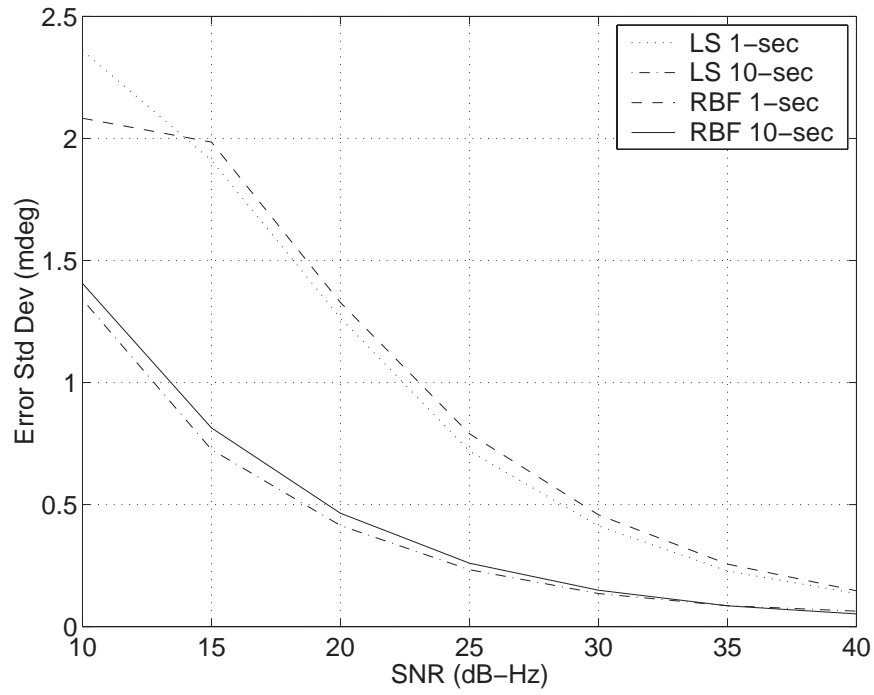


Figure 16: Error standard deviations $EL\ 45^\circ$

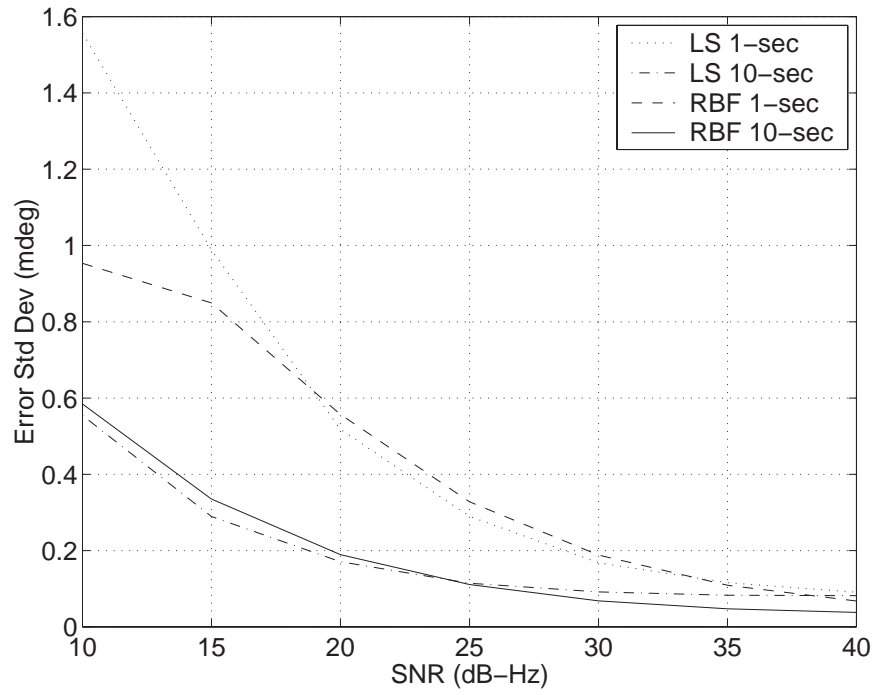


Figure 17: Error standard deviations $XEL\ 75^\circ$

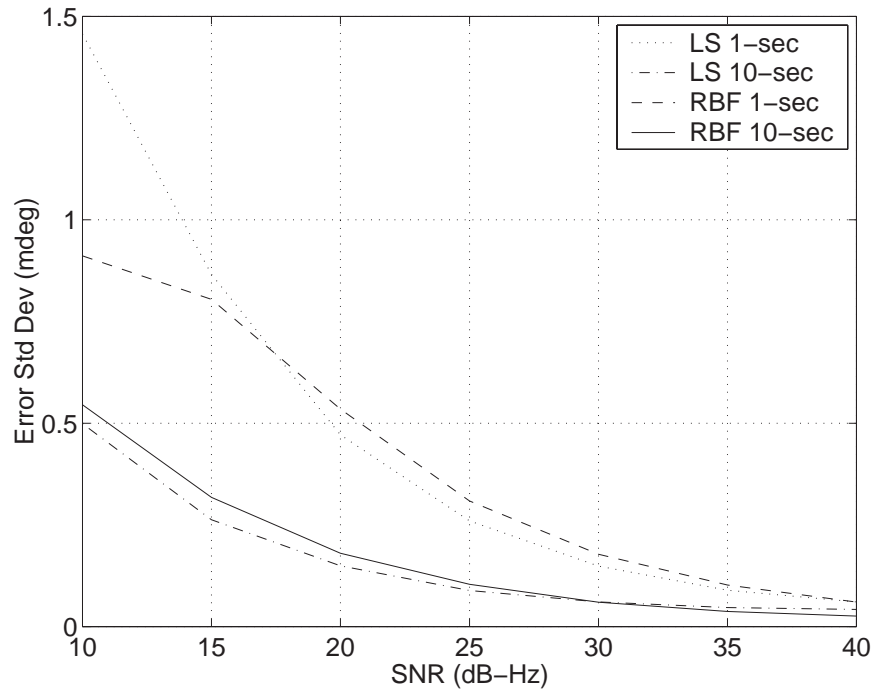


Figure 18: Error standard deviations $EL\ 75^\circ$

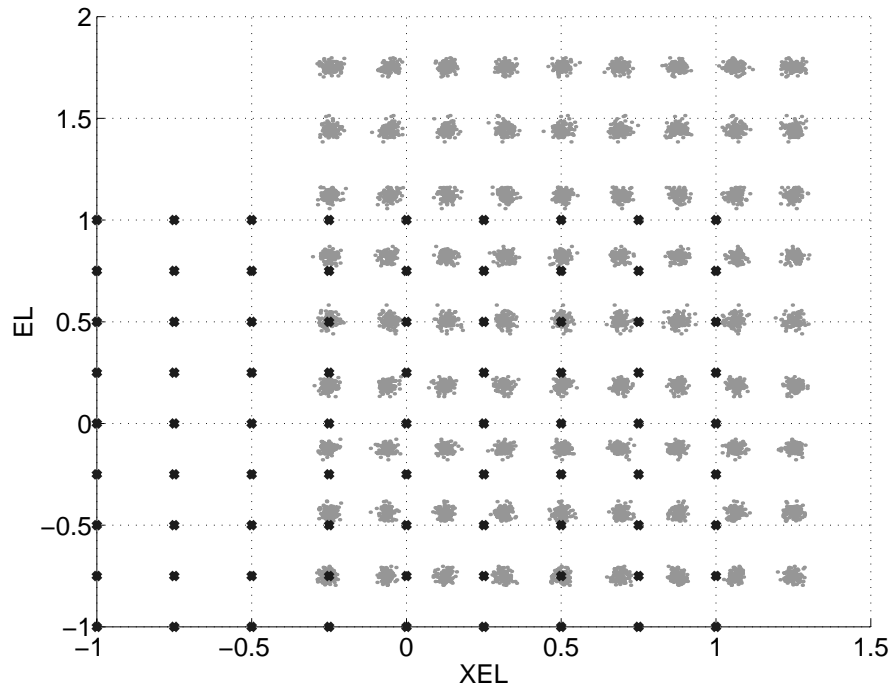


Figure 19: Performance of RBF network trained on old data at 75°

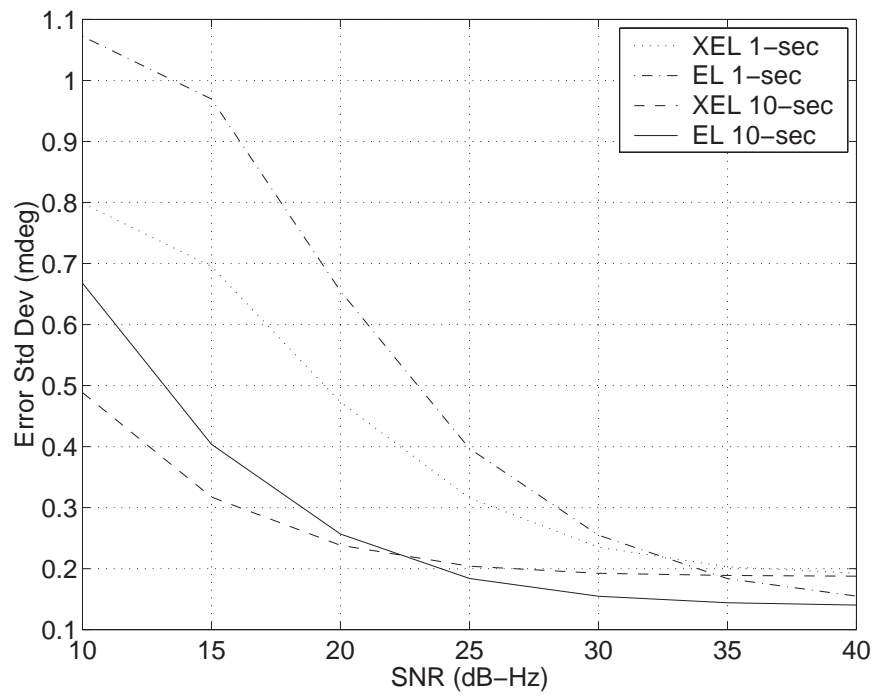


Figure 20: Error standard deviation resulting from training on old data: 75°

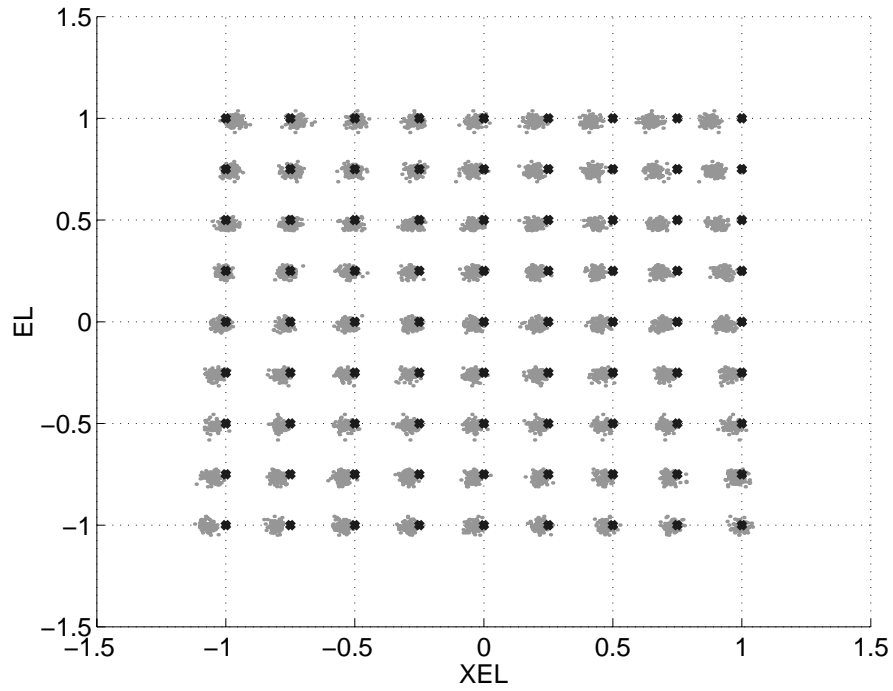


Figure 21: Performance of RBF network adapted with the LMS algorithm at 75°

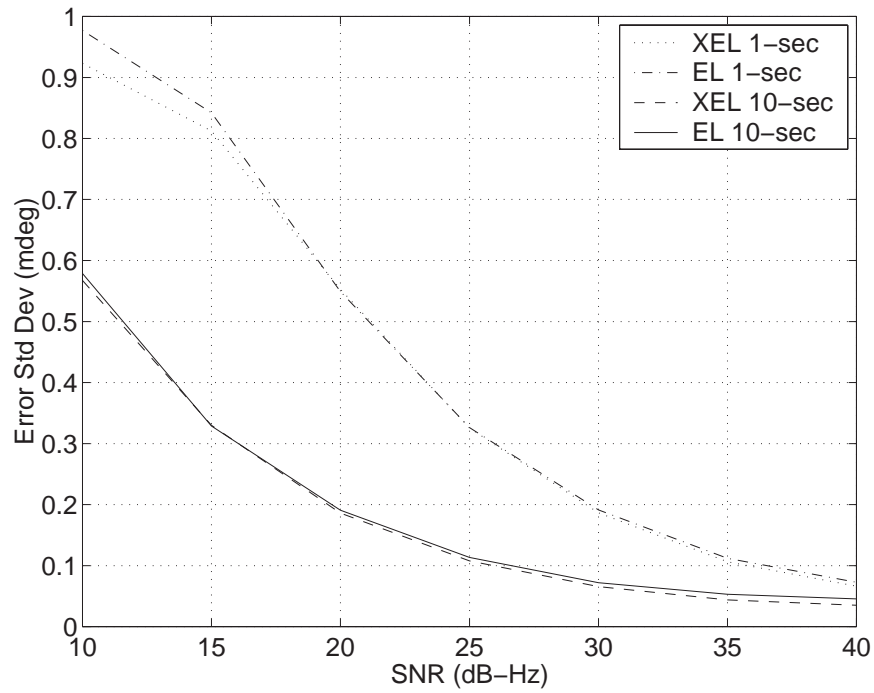


Figure 22: Error Standard Deviation after LMS adaptation

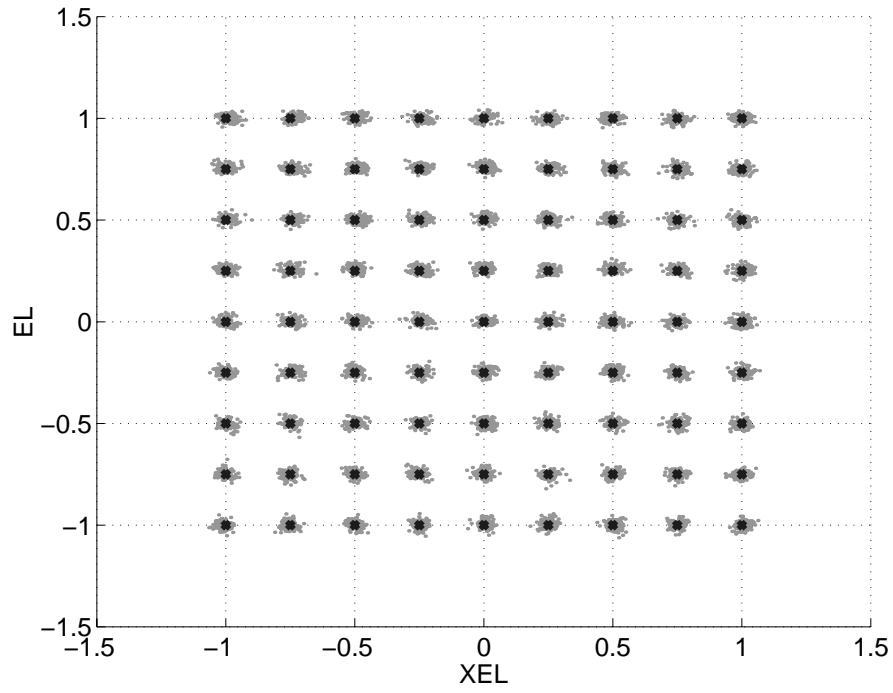


Figure 23: Performance of RBF network adapted using the pseudo-inverse method at 75°

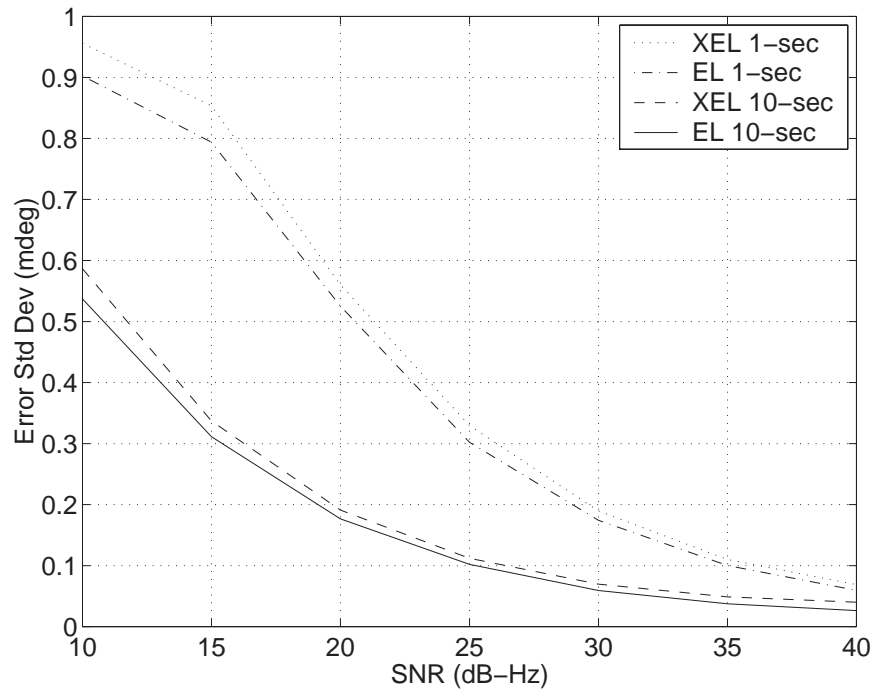


Figure 24: Error standard deviations after pseudo-inverse re-training

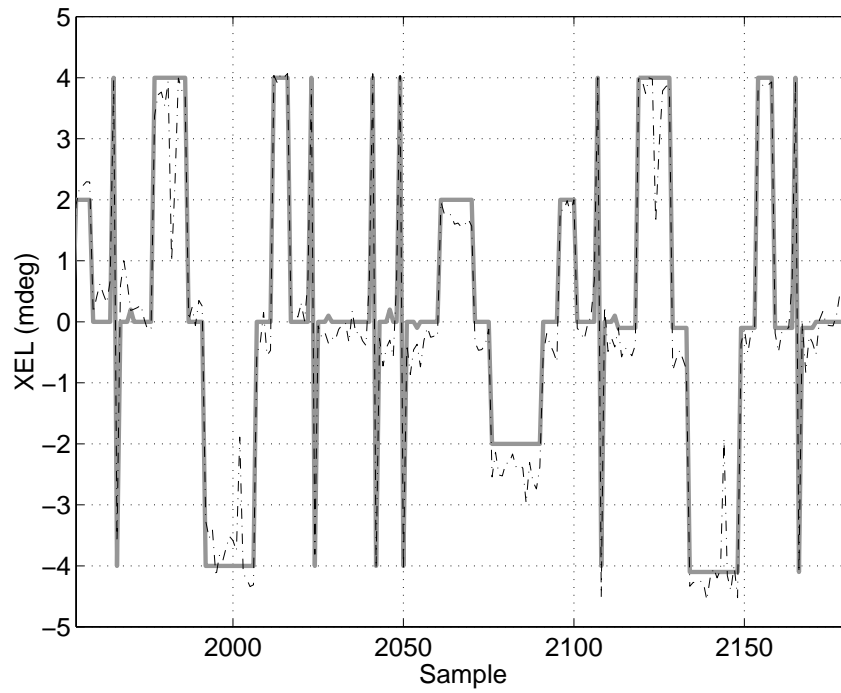


Figure 25: Day 29 *XEL* estimation over Region 3

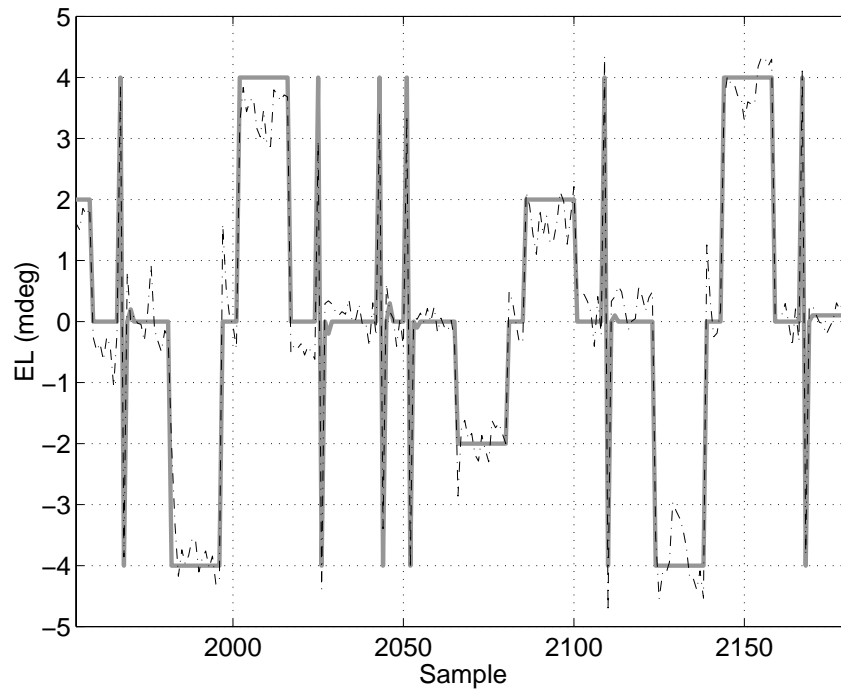


Figure 26: Day 29 *EL* estimation over Region 3